RESEARCH ARTICLE

ADVANCED OPTICAL MATERIALS
www.advopticalmat.de

Resonant Fully Dielectric Metasurfaces for Ultrafast Terahertz Pulse Generation

Luke Peters, Davide Rocco, Luana Olivieri, Unai Arregui Leon, Vittorio Cecconi, Luca Carletti, Carlo Gigli, Giuseppe Della Valle, Antonio Cutrona, Juan Sebastian Totero Gongora, Giuseppe Leo, Alessia Pasquazi, Costantino De Angelis, and Marco Peccianti**

Metasurfaces represent a new frontier in materials science paving for unprecedented methods of controlling electromagnetic waves, with a range of applications spanning from sensing to imaging and communications. For pulsed terahertz (THz) generation, metasurfaces offer a gateway to tuneable thin emitters that can be utilized for large-area imaging, microscopy, and spectroscopy. In literature, THz-emitting metasurfaces generally exhibit high absorption, being based either on metals or on semiconductors excited in highly resonant regimes. Here, the use of a fully dielectric semiconductor exploiting morphology-mediated resonances and inherent quadratic nonlinear response is proposed. This system exhibits a remarkable 40-fold efficiency enhancement compared to the unpatterned at the peak of the optimized wavelength range, demonstrating its potential as a scalable emitter design.

L. Peters, L. Olivieri, V. Cecconi, A. Cutrona, J. S. Totero Gongora, A. Pasquazi, M. Peccianti
Emergent Photonics Research Centre
Dept. of Physics
Loughborough University
Loughborough LE11 3TU, UK
E-mail: l.peters@lboro.ac.uk; m.peccianti@lboro.ac.uk

L. Peters, L. Olivieri, A. Cutrona, J. S. Totero Gongora, A. Pasquazi, M. Peccianti
Emergent Photonics Lab (Epic)
Department of Physics and Astronomy
University of Sussex
Brighton BN1 9QH, UK

D. Rocco, L. Carletti, C. De Angelis
Department of Information Engineering
University of Brescia
via Branze 38, Brescia 25123, Italy

U. Arregui Leon, G. Della Valle
Politecnico di Milano
Department of Physics
Piazza Leonardo Da Vinci 32, Milan 20133, Italy

C. Gigli, G. Leo
Matériaux et Phénomènes Quantiques
Université Paris Cité and CNRS
10 rue A. Domon et L. Duquet, Paris 75013, France

The ORCID identification number(s) for the author(s) of this article can be found under https://doi.org/10.1002/adom.202303148

DOI: 10.1002/adom.202303148

1. Introduction

Optical metasurfaces, the 2D counterpart of metamaterials, have emerged as a compelling area of research in photonics. In general terms, metasurfaces are densely engineered surfaces and are often composed of arrays of subwavelength structures where the field is manipulated by different physical local processes. Research has been motivated by the promise of manipulating light in novel fashions, thereby opening up new avenues for optical functionalities.[1] The studies in this particular area are driven by the aspiration to develop metasurface-based devices that can ensure efficient, compact, and on-chip frequency conversion, steering the future of photonics towards a more integrated and functional landscape, with very strong use cases beginning to enter the mainstream, ranging from flat-optics cameras on mobile phones[2] to wave-front engineering for telecommunications.[3] Within the framework of the nonlinear frequency conversion, that is, the generation of new optical frequencies via a nonlinear field-matter interaction, metasurfaces are assuming a quite intriguing pivotal role, as they offer a unique platform to enhance the nonlinear optical processes, overcoming the limitations posed by conventional nonlinear materials such as phase-matching constraints and low conversion efficiencies.[4–6] The investigation of these concepts within the terahertz (THz) frequency spectrum is quite recent. General research on terahertz light, which occupies the 0.1 to 10 THz band of the electromagnetic spectrum, is fuelled by fundamental and practical ramifications in fields as different as biological imaging,[7–9] art restoration,[10–12] and telecommunications.[13–15] Indeed, the nonlinear generation of terahertz pulses from ultrafast optical sources is indeed standard in the field[16–18] and it is historically considered a seminal achievement enabling the modern terahertz research area. However, the lack of efficient large-area thin emitters is certainly a fundamental and practical limit, bringing cumbersome experimental setups with complex geometries as well as several other limitations like the resolution limits of novel near-field imaging systems.[19–23] Research on ultrathin emitters brought the investigation of surfaces because of the rich nonlinear optical phenomenology hosted[24–27] and also to the exploration of novel physical mechanisms as in the emerging class of spintronic emitters[28–30] with

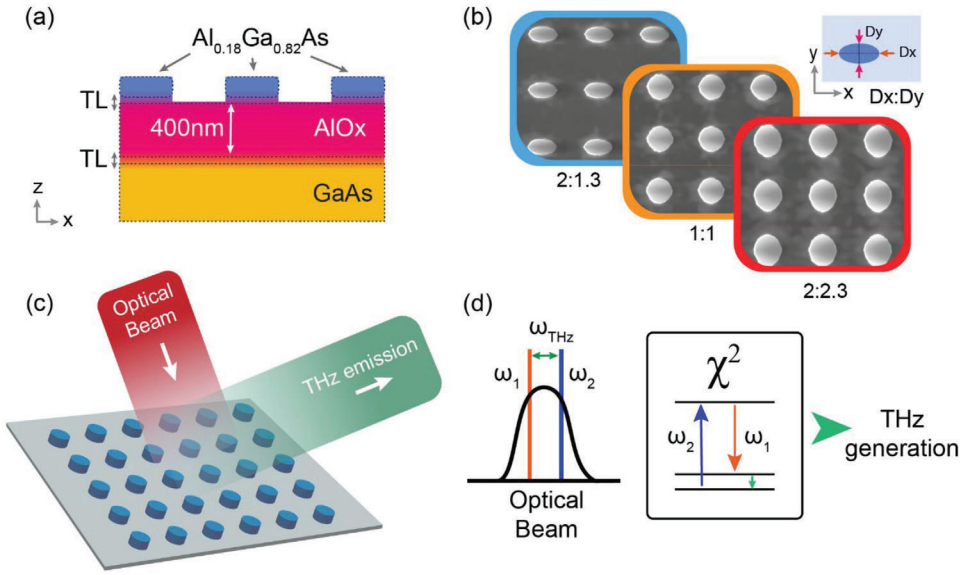

Figure 1. Terahertz generation mechanism in resonant dielectric metasurfaces. a) Sketch of the metasurface's composition: AlGaAs elements over a 400-nm-thick AlOx substrate. TL – transition layers 90-nm-thick. b) SEM insets of the metasurfaces' spatial distribution (full SEM images available in Figure S1, Supporting Information). The metasurfaces are named after the ratio Dx:Dy. The 1:1 design has a circular base with a 190-nm radius, 2:1.3 has dimensions of 384 by 207 nm, and 2:2.3 measures 380 by 437 nm. c) Conceptual sketch of the THz generation process. d) Diagram of the intrapulse optical rectification process.

exceptional conversion efficiency per unit of thickness. However, in those technologies, the ability to tailor the emission in regards to the nature of the excitation and the spatiotemporal property of the emitted waves is quite limited. As a result, we expect metasurfaces to play a growing role in this area.[31–33]

Among the platforms proposed in the community, metal-based metasurfaces[34–36] offer a relatively strong nonlinear response boosted by local field enhancement without the several challenges related to the typical velocity matching condition required in bulk generation. Metal high ohmic losses at optical frequencies are the typical drawback that affects nonlinear conversion efficiencies.[37,38]

More exotic metasurface platforms include: Randomly distributed nanotips such as "black-silicon"[39,40], and "quasi-bound in continuum (BIC)" materials.[41] Although these results demonstrate enhanced THz generation, they seldom offer a means of customizing emission parameters, such as phase, wavelength, and bandwidth. In addition, quasi-BIC exploits narrowband resonances which also might affect typical terahertz use cases. Recently, terahertz generation from above-bandgap excited semiconductor metasurfaces has been demonstrated[42] in the absorption regime. The generation exceeds the one from the native substrate, usually driven by a combination of different surface phenomena, for example, surface quadratic nonlinearities, carrier drift, photo-Dember processes,[43] and the bulk nonlinear response.

Drawing insights from purely theoretical studies on THz generation from individual all-dielectric nanoantennas dominated by Mie resonances in the infrared[44], here we present AlGaAs metasurfaces tailored for pulsed terahertz generation from an extended system, which similarly employs dielectrics to mitigate conversion losses.[44–46]

2. Methodology and Results

The metasurfaces comprise a 400-nm tall nanocylinder of Al0.18Ga0.82As fabricated using electron-beam lithography. These cylinders are placed on a 400 nm thick AlOx substrate with a low refractive index ($n = 1.6$) (**Figure 1a**). The fabrication process is detailed in the Experimental Section.

We examined three different designs characterized by a 2D array of nanocylinders with an elliptical cross-section, each with distinct ellipticities Dx:Dy, where Dx and Dy are the axes of the elliptical base Figure 1b displays an inset for the 2:1.3, 1:1, and 2:2.3 ellipticity metasurfaces. Specifically, the 1:1 design has a circular base with a 190 nm radius, 2:1.3 has dimensions of 384 by 207 nm, and 2:2.3 measures 380 by 437 nm. The period of the 2D array is 750 nm. Comprehensive SEM images can be found in the Supporting Information (Figure S1, Supporting Information).

The samples are analyzed using a standard reflection geometry, employing a high-energy optical beam for the nonlinear generation of THz radiation as schematically sketched in (Figure 1c). The structures are tailored to maximize internal energy for the optical input wavelength, ≈1280 nm (below-bandgap), and for a *p*-polarized coupling at a 45° optical impinging angle with respect to the surface plane.

As the structure offers negligible absorption (unlike for example typical surface generation in low-bandgap III–V semiconductors), the generation is mediated by a quadratic field-matter interaction mechanism that drives an optical rectification process, as in many THz nonlinear crystals[45] (Figure 1d).

3D finite element simulations of the metasurfaces were used to correlate the different ellipticities with the spectrum of the internal energy (see **Figure 2a–d**, more information in Experimental Section), highlighting a predominant resonance around the pump wavelength (1280 nm) for the sample 2:2.3.

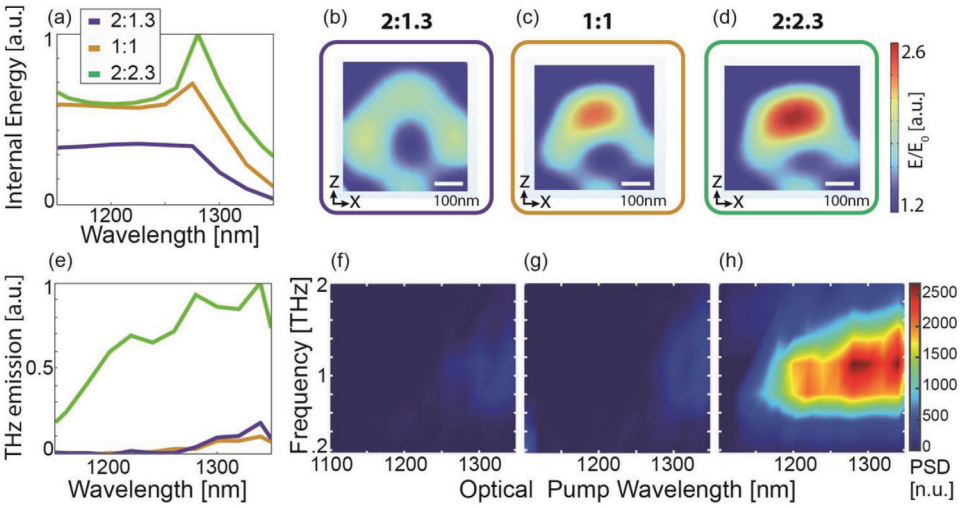

Figure 2. Study on terahertz emission from the dielectric metasurfaces. a) Simulated total internal energy for the different metamaterials. b–d) The simulated field enhancement inside the meta-atoms that form the different metasurfaces 2:1.3, 1:1, and 2:2.3 respectively represents the amplitude of the incidence field. e) THz experimental contribution from the nanoparticles as a function of the optical pump wavelength. f–h) THz experimental emission from the 2:1.3, 1:1, and 2:2.3 metasurfaces respectively, results are shown in the frequency domain, where PSD is power spectral density. Note (e–h) are obtained by subtracting the substrate contribution.

Terahertz emission efficiency was tested via focussed ultrafast femtosecond pulse illumination, with a spot diameter in the order of 50 μm. We note that this investigation focuses on the *p*-polarization as optimal for the chosen experimental design. Figure 2f–h presents the general feature of the emission at different pump center wavelengths and for different aspect ratios of the structure, in the range of 1100–1350 nm. Notably, the contribution of the substrate to emission was also measured (reported in Figure S2, Supporting Information for completeness) and removed from the characterization of the metasurfaces. The terahertz power emission dependence from the illumination reflects the quadratic response of the medium in the experimental regime considered.

The theoretical modeling predicts an enhancement of the total internal energy for nanoparticles with a longer axis parallel to the terahertz polarization direction (2:2.3 design) around the optical pump wavelength of 1280 nm (Figure 2a,d). This alignment allows the optical field to couple more effectively to dielectric resonances along the longer nanoparticle axis, boosting the internal field intensity. A larger internal field enables greater nonlinear optical rectification, leading to higher terahertz emission efficiency. Notably, beyond 1280 nm, the experimental results deviate from the modeling predictions (Figure 2a,e). This discrepancy arises most likely because the simulations account only for nonlinear generation within the metasurface nanoparticles, neglecting substrate contributions.

The experiments clearly evidence a significant boost in terahertz emission from the 2:2.3 metasurfaces at 1280 nm (Figure 2e,h). Across the full span of pump wavelengths tested, this elongated nanoparticle design maintains higher conversion efficiency, validating the enhanced performance of this metasurface configuration. This is additionally confirmed by the nonlinear simulations (reported in Figure S3, Supporting Information). Remarkably, a 40-fold increase in the total detected energy is observed when comparing metasurface 2:2.3 (Figure 2h) to the base substrate (Figure S3a, Supporting Information) at a pump wavelength of 1400 nm. For the designed resonance peak at 1280 nm, an enhancement of around 15 times is seen.

Although the other two metasurface geometries produce lower terahertz yields, they reveal quite intriguing emission dynamics. Terahertz time-domain spectra for each design at various optical wavelengths (**Figure 3**a–c) show a distinct change in the carrier-envelope phase of the pulse emitted.

In a further investigation, we plot the terahertz phase for the different metasurfaces across a range of pump wavelengths and terahertz frequencies (Figure 3d–f). Remarkably, these broadband resonant nanostructures enable continuous control over the emitted terahertz phase profile simply by acting upon the metasurface shape and pump wavelength. We remark that this could allow a route toward wavefront engineering, which is a sharp challenge in the broadband terahertz domain.

3. Conclusion

In conclusion, this work demonstrates broadband all-dielectric metasurfaces for efficient, customizable terahertz pulse generation. The proposed structure comprises cylindrical semiconductor nanoresonators based on the AlGaAs/GaAs platform. Through optimization of the metasurface design, a significant 40-fold enhancement in terahertz emission efficiency is achieved compared to the bare substrate. Intriguing, beyond the efficiency, the structure enables a form of control over the emitted terahertz radiation characteristics. By tailoring the shape and dimensions of the nanocylinder elliptical cross-section, the amplitude and the phase profile of the resulting terahertz pulses can be changed. The structures enable manipulation of the terahertz phase by merely tuning the optical excitation wavelength. This peculiar capacity for spatio-temporal structuring of the terahertz wavefront at a planar nanophotonic interface could empower different types of applications. These include ultrafast terahertz beam

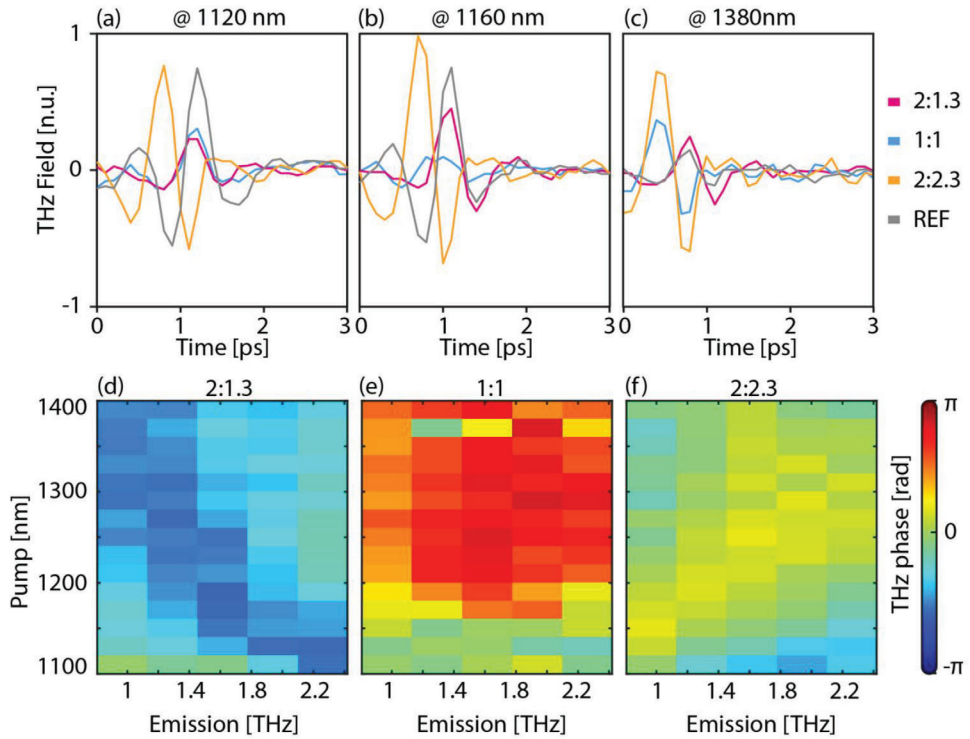

Figure 3. Phase of terahertz emissions from the dielectric metasurfaces. a–c) THz-TDS traces obtained from the metasurfaces, for varying different input wavelengths (1120, 1160, and 1380 nm respectively), showing the difference in the phase of the THz emission. d–f) Map diagrams for each of the three metasurfaces for varying input wavelengths and THz frequencies. Note that for comparison the phase of the absolute phase of the bottom left corner is set to 0 to highlight the dynamics. The reference signal is generated from the substrate without the dielectric metasurface. The initial temporal position of the pulse is not conserved changing the sample.

steering, wireless communication, computational imaging, and spectroscopy. More broadly, the approach highlights the potential of all-dielectric metasurfaces for nonlinear frequency conversion, circumventing limitations of plasmonic systems and, more in general, non-transparent systems. With further optimization, such engineered nanoresonator surfaces may displace traditional bulk crystals for terahertz generation. Looking beyond, the concepts demonstrated here are a potential route to unlock the full potential of metasurfaces in terahertz photonics.

4. Experimental Section

Fabrication: Sample fabrication was based on a molecular beam epitaxy growth substrate with the following layered structure: i) [100] non-intentionally doped GaAs wafer, ii) 90 nm of GaAs-to-Al0.98Ga0.02As transition layer with linearly increasing Al concentration, iii) 1 µm of Al0.98Ga0.02As, 90 nm of Al0.98Ga0.02As-to-Al0.18Ga0.82As transition layer with linearly decreasing Al concentration, iv) 400 nm of Al0.18Ga0.82As. For the adhesion layer, a 10-nm layer of SiO2 was deposited using plasma-enhanced chemical vapor deposition (PECVD). This was complemented by a spin-coated 100-nm layer of hydrogen silsesquioxane (HSQ) serving as a negative resist. The desired metasurface geometry was patterned through 20 kV e-beam lithography and transferred to the AlGaAs layer by inductively coupled plasma-reactive-ion etching (ICP- RIE) with SiCl4:Ar chemical treatment. Finally, wet oxidation was performed in an oven at 390 °C for 40 min under a controlled mix of water vapor and N2:H2 gas carrier aiming at converting the 1 µm Al-rich layer into amorphous non-stoichiometric aluminum oxide (AlOx).

Experimental Setup: The experimental setup consisted of a Chameleon ultrafast laser, equipped with a compact OPO (optical parametric oscillator) attachment. The laser offered a repetition rate of 80 MHz, a pulse duration of 140 fs before the OPO, and an average power of 4 W before the OPO. The OPO allowed for the variability in the wavelength. The OPO impinging power on the structure was around 150 mW. This laser directed a conventional THz-TDS setup and configured for reflection-generation spectroscopy. Notably, the detection crystal employed was a 1mm-thick Zinc Telluride. The ZnTe was rotated to selectively detect *p*-polarized input light (with polarization lying in the plane containing impinging and reflected rays).[46] The detection was performed via optical sampling supplied directly with the Chameleon laser line at a wavelength of 850 nm (close to optimal collinear phase-matching condition in ZnTe). Diagrams detailing the experimental setting are available in the Supporting Information (Figure S4, Supporting Information).

Theoretical Simulations: 3D finite element method simulations were performed in COMSOL Multiphysics. The metasurfaces of AlGaAs nanoresonators were modeled on a substrate, applying Floquet boundary conditions to emulate an infinite periodic structure. The refractive index dispersion of AlGaAs was taken into account according to ref. [44].

The primary excitation was modeled as a plane wave *p*-polarized with an incident angle of 45° with respect to the surface face. Both linear and nonlinear calculations were performed. Due to the significant difference in length scales between the optical (a few µm) and THz domains (hundreds to thousands of µm), the simulation incorporated two components with distinct domain dimensions. One component ensured a well-meshed model in the optical domain, featuring a refined mesh for the nano-cylindrical resonators. In contrast, the other component accommodated at least one wavelength in the THz regime.

As mentioned in ref. [44], a general extrusion coupling operator was implemented to correlate the nanocylinders of both components. This process mapped electromagnetic fields in the optical wavelengths in the destination geometry (THz range) by keeping the same finer mesh inside the resonators and relaxing the mesh in the surrounding domains, effectively optimizing computational resource utilization.

For the incident beam, the model was based on a Gaussian pulse centered at 2.34 THz (≈1280 nm) with a bandwidth of 2 THz, defined as the spectral width at 1/e2 of the spectral peak. To assess the complete THz emission from the metasurface, a discretized spectrum of the incident Gaussian beam was employed. It was sampled with a discrete set of frequency steps ($N = 18$, each step ≈0.118 THz apart), enabling the calculation of difference-frequency generation (DFG) between the weighted spectral components. This approach condensed the simulations of the total THz generation into several DFG problems which could be modeled following ref. [44], where only the bulk nonlinearities were considered. For given incident fields spectral components (E(ω1), E(ω2)) with their relative amplitude weight, we use Equation (1) for obtaining the DFG nonlinear current densities J_i at $\omega n = \omega 2 - \omega 1$.

$$J_i(\omega_n) = -i\omega_n \varepsilon_0 \chi^{(2)}_{ijk}(\omega_n; \omega_2, -\omega_1)\left[E_j(\omega_2) E^*_k(\omega_1) + E_k(\omega_2) E^*_j(\omega_1)\right] \quad (1)$$

where ϵ_0 is the vacuum permittivity and $\chi(2)$ denotes the frequency-dependent AlGaAs nonlinear susceptibility tensor, i≠j≠k being the Cartesian coordinates. The nonlinear currents imposed within the AlGaAs nanocylinder were the sources for the nonlinear DFG field. For every spectral component (with N frequency components of the incident Gaussian beam), the DFG contributions for all combinations were calculated, resulting in $N(N-1)/2$ simulations.

Lastly, the final THz signal component at ω_n was computed as the sum of all the DFG contributions that generated the nonlinear THz signal at that specific ω_n (where $\omega_n = n \cdot \Delta f$ with $n = 1,...,N-1$). The obtained results were in substantial agreement with the experimental measurement. Hence, the simplified computational framework proposed here was able to catch all the main features concerning the THz emission from dielectric metasurfaces. It was important to emphasize that only bulk nonlinearities were considered in the simulations. As shown theoretically in ref. [44], the THz efficiency notably improved around the AlGaAs phonon polariton frequencies (≈8 and ≈11 THz). Consequently, leveraging incident pump signals with an expansive frequency band could offer additional advantages in enhancing nonlinear efficiency.

Supporting Information

Supporting Information is available from the Wiley Online Library or from the author.

Acknowledgements

This project received funding from the European Research Council (ERC) under the European Union's Horizon 2020 Research and Innovation Programme grant no. 725046 as well from the UK Engineering and Physical Sciences Research Council (EPSRC), grant no. EP/W028344/1, The Leverhulme Trust Early Career Fellowship Early Career Fellowship (ECF-2022-710 and ECF-2023-315) as well as the Leverhulme Trust Research Project grant RPG-2022-090. This work was supported by European union - Next generation EU through PRIN 2022 project GRACE6G (2022H7RR4F), PRIN PRR 2022 project FLAIRS (P2022RFF9K) and PRIN 2020 project METEOR (2022EY2LJT_002). This publication is part of the METAFAST project that received funding from the European Union Horizon 2020 Research and Innovation Programme under Grant Agreement No. 899673. This work reflects only the authors' views, and the European Commission is not responsible for any use that may be made of the information it contains. G.L. thanks Aristide Lemaître for the epitaxial growth of the sample.

Conflict of Interest

The authors declare no conflict of interest.

Data Availability Statement

The data that support the findings of this study are openly available at https://repository.lboro.ac.uk/ at https://doi.org/10.17028/rd.lboro.24787806, reference number 24787806.

Keywords

dielectric, metasurfaces, terahertz

Received: December 11, 2023
Revised: March 20, 2024
Published online:

[1] N. Yu, P. Genevet, M. A. Kats, F. Aieta, J.-P. Tetienne, F. Capasso, Z. Gaburro, *Science* **2011**, *334*, 333.
[2] O. Reshef, M. P. DelMastro, K. K. M. Bearne, A. H. Alhulaymi, L. Giner, R. W. Boyd, J. S. Lundeen, *Nat. Commun.* **2021**, *12*, 3512.
[3] Z. Wang, T. Li, A. Soman, D. Mao, T. Kananen, T. Gu, *Nat. Commun.* **2019**, *10*, 3547.
[4] A. V. Kildishev, A. Boltasseva, V. M. Shalaev, *Science* **2013**, *339*, 1232009.
[5] S. Liu, M. B. Sinclair, S. Saravi, G. A. Keeler, Y. Yang, J. Reno, G. M. Peake, F. Setzpfandt, I. Staude, T. Pertsch, I. Brener, *Nano Lett.* **2016**, *16*, 5426.
[6] A. Di Francescantonio, A. Zilli, D. Rocco, L. Coudrat, F. Conti, P. Biagioni, L. Duò, A. Lemaître, C. De Angelis, G. Leo, M. Finazzi, M. Celebrano, *Nat. Nanotechnol.* **2023**, *19*, 298.
[7] Q. Sun, Y. He, K. Liu, S. Fan, E. P. J. Parrott, E. Pickwell-MacPherson, *Quant. Imaging Med. Surg.* **2017**, *7*, 34555.
[8] E. Pickwell, B. E. Cole, A. J. Fitzgerald, M. Pepper, V. P. Wallace, *Phys. Med. Biol.* **2004**, *49*, 1595.
[9] P. C. Ashworth, E. Pickwell-MacPherson, E. Provenzano, S. E. Pinder, A. D. Purushotham, M. Pepper, V. P. Wallace, *Opt. Express* **2009**, *17*, 12444.
[10] C. Seco-Martorell, V. López-Domínguez, G. Arauz-Garofalo, A. Redo-Sanchez, J. Palacios, J. Tejada, *Opt. Express* **2013**, *21*, 17800.
[11] L. Öhrström, B. M. Fischer, A. Bitzer, J. Wallauer, M. Walther, F. Rühli, *Anat. Rec.* **2015**, *298*, 1135.
[12] G. Leong, M. Brolly, P. Taday, D. Giovannacci, presented at 2022 47th Int. Conf. on Infrared, Millimeter and Terahertz Waves (IRMMW-THz), Delft, Netherlands, August **2022**.
[13] T. Nagatsuma, G. Ducournau, C. C. Renaud, *Nat. Photonics* **2016**, *10*, 371.
[14] H. Elayan, O. Amin, B. Shihada, R. M. Shubair, M.-S. Alouini, *IEEE Open J. Commun. Soc.* **2020**, *1*, 1.
[15] A. E. Willner, X. Su, H. Zhou, A. Minoofar, Z. Zhao, R. Zhang, M. Tur, A. F. Molisch, D. Lee, A. Almaiman, *J. Opt.* **2022**, *24*, 124002.
[16] K. H. Yang, P. L. Richards, Y. R. Shen, *Appl. Phys. Lett.* **1971**, *19*, 320.
[17] G. Mourou, C. V. Stancampiano, A. Antonetti, A. Orszag, *Appl. Phys. Lett.* **1981**, *39*, 295.
[18] D. H. Auston, K. P. Cheung, J. A. Valdmanis, D. A. Kleinman, *Phys. Rev. Lett.* **1984**, *53*, 1555.
[19] F. Blanchard, A. Doi, T. Tanaka, H. Hirori, H. Tanaka, Y. Kadoya, K. Tanaka, *Opt. Express* **2011**, *19*, 8277.
[20] J. S. Totero Gongora, L. Olivieri, L. Peters, J. Tunesi, V. Cecconi, A. Cutrona, R. Tucker, V. Kumar, A. Pasquazi, M. Peccianti, *Micromachines* **2020**, *11*, 521.

[21] L. Olivieri, J. S. T. Gongora, L. Peters, V. Cecconi, A. Cutrona, J. Tunesi, R. Tucker, A. Pasquazi, M. Peccianti, *Optica* **2020**, *7*, 186.
[22] L. Olivieri, L. Peters, V. Cecconi, A. Cutrona, M. Rowley, J. S. Totero Gongora, A. Pasquazi, M. Peccianti, *ACS Photonics* **2023**, *10*, 1726.
[23] L. L. Hale, T. Siday, O. Mitrofanov, *Opt. Mater. Express* **2023**, *13*, 3068.
[24] P. Gu, M. Tani, S. Kono, K. Sakai, X.-C. Zhang, *J. Appl. Phys.* **2002**, *91*, 5533.
[25] M. Reid, R. Fedosejevs, *Appl. Phys. Lett.* **2005**, *86*, 011906.
[26] A. Krotkus, R. Adomavičius, G. Molis, V. L. Malevich, *J. Nanoelectron. Optoelectron.* **2007**, *2*, 108.
[27] L. Peters, J. Tunesi, A. Pasquazi, M. Peccianti, *Nano Energy* **2018**, *46*, 128.
[28] T. Kampfrath, M. Battiato, P. Maldonado, G. Eilers, J. Nötzold, S. Mährlein, V. Zbarsky, F. Freimuth, Y. Mokrousov, S. Blügel, M. Wolf, I. Radu, P. M. Oppeneer, M. Münzenberg, *Nat. Nanotechnol.* **2013**, *8*, 256.
[29] T. Seifert, S. Jaiswal, U. Martens, J. Hannegan, L. Braun, P. Maldonado, F. Freimuth, A. Kronenberg, J. Henrizi, I. Radu, E. Beaurepaire, Y. Mokrousov, P. M. Oppeneer, M. Jourdan, G. Jakob, D. Turchinovich, L. M. Hayden, M. Wolf, M. Münzenberg, M. Kläui, T. Kampfrath, *Nat. Photonics* **2016**, *10*, 483.
[30] C. Bull, S. M. Hewett, R. Ji, C.-H. Lin, T. Thomson, D. M. Graham, P. W. Nutter, *APL Mater.* **2021**, *9*, 090701.
[31] M. Tal, S. Keren-Zur, T. Ellenbogen, *ACS Photonics* **2020**, *7*, 3286.
[32] S. Keren-Zur, O. Avayu, L. Michaeli, T. Ellenbogen, *ACS Photonics* **2016**, *3*, 117.
[33] S. Keren-Zur, M. Tal, S. Fleischer, D. M. Mittleman, T. Ellenbogen, *Nat. Commun.* **2019**, *10*, 1778.
[34] H. Cai, Q. Huang, X. Hu, Y. Liu, Z. Fu, Y. Zhao, H. He, Y. Lu, *Adv. Opt. Mater.* **2018**, *6*, 1800143.
[35] J. Lee, M. Tymchenko, C. Argyropoulos, P.-Y. Chen, F. Lu, F. Demmerle, G. Boehm, M.-C. Amann, A. Alù, M. A. Belkin, *Nature* **2014**, *511*, 65.
[36] M. S. Bin-Alam, O. Reshef, Y. Mamchur, M. Z. Alam, G. Carlow, J. Upham, B. T. Sullivan, J.-M. Ménard, M. J. Huttunen, R. W. Boyd, K. Dolgaleva, *Nat. Commun.* **2021**, *12*, 974.
[37] A. Vora, J. Gwamuri, N. Pala, A. Kulkarni, J. M. Pearce, D. Ö. Güney, *Sci. Rep.* **2014**, *4*, 4901.
[38] J. B. Khurgin, *Philos. Trans. R. Soc., A* **2017**, *375*, 20160068.
[39] J. Tunesi, L. Peters, J. S. Totero Gongora, L. Olivieri, A. Fratalocchi, A. Pasquazi, M. Peccianti, *Phys. Rev. Res.* **2021**, *3*, L042006.
[40] U. Blumröder, M. Zilk, H. Hempel, P. Hoyer, T. Pertsch, R. Eichberger, T. Unold, S. Nolte, *Opt. Express* **2017**, *25*, 6604.
[41] L. Hu, B. Wang, Y. Guo, S. Du, J. Chen, J. Li, C. Gu, L. Wang, *Adv. Opt. Mater.* **2022**, *10*, 2200193.
[42] L. L. Hale, H. Jung, S. D. Gennaro, J. Briscoe, C. T. Harris, T. S. Luk, S. J. Addamane, J. L. Reno, I. Brener, O. Mitrofanov, *ACS Photonics* **2022**, *9*, 1136.
[43] L. Peters, J. Tunesi, A. Pasquazi, M. Peccianti, *Sci. Rep.* **2017**, *7*, 9805.
[44] U. A. Leon, D. Rocco, L. Carletti, M. Peccianti, S. Maci, G. D Valle, C. De Angelis, *Sci. Rep.* **2022**, *12*, 4590.
[45] M. A. A. Rice, Y. Jin, X. F. Ma, X.-C. Zhang, D. Bliss, J. Larkin, *Appl. Phys. Lett.* **1994**, *64*, 1324.
[46] P. C. M. Planken, H.-K. Nienhuys, H. J. Bakker, T. Wenckebach, *J. Opt. Soc. Am. B* **2001**, *18*, 313.